RSC Advances

ROYAL SOCIETY OF CHEMISTRY

PAPER

View Article Online
View Journal | View Issue

Cite this: *RSC Adv.*, 2019, **9**, 41591

Construction of novel Ag/HKUST-1/g-C_3N_4 towards enhanced photocatalytic activity for the degradation of pollutants under visible light†

Yu Qiao,[ab] Qian Han,[a] Dong Li,[d] Hongji Li,[a] Bing Wei,[c] Guangbo Che,*[a] Wei Jiang[a] and Weisheng Guan*[b]

Received 17th October 2019
Accepted 20th November 2019

DOI: 10.1039/c9ra08489d

rsc.li/rsc-advances

A novel Ag/metal–organic framework/graphitic carbon nitride (Ag/HKUST-1/g-C_3N_4, AHC) photocatalyst was prepared *via* an *in situ* growth strategy and photo-deposition technique for environmental remediation. The as-obtained samples were characterized by X-ray diffraction (XRD), transmission electron microscopy (TEM), scanning electron microscopy (SEM), X-ray photoelectron spectroscopy (XPS), N_2 adsorption–desorption isotherm measurement, UV-vis diffuse reflection spectroscopy (UV-vis DRS), and photoluminescence (PL) spectroscopy. The results indicated that the hybrids have large surface area, mesoporous structure and enhanced visible-light absorption. The as-prepared hybrid samples exhibited considerable improvement in photocatalytic activity and stability for rhodamine B (RhB) degradation under visible light irradiation ($\lambda > 420$ nm). In addition, they also have good adsorption properties. Compared to the pure g-C_3N_4 and Ag/g-C_3N_4, the 5% AHC photocatalyst showed superior photocatalytic activity. Moreover, 5% AHC exhibits good photocatalytic activity even after four cycles. Additionally, the active species trapping and electron spin resonance (ESR) experiments indicated that h^+ and ·OH were the main active species.

Introduction

With environmental degradation becoming increasingly prominent throughout the world, the effective control of environmental pollutants and government intervention have become urgent to address this issue. During the past decade, a variety of strategies have been employed to solve this problem.[1–3] The semiconductor photocatalytic technique using the renewable solar energy to degrade organic pollutants to non-toxic products has received word-wide attention.[4] Simultaneously, visible-light-driven photocatalysts have attracted considerable attention because sunlight consists of about 50% visible light and only about 4% ultraviolet (UV) light. Additionally, nanomaterials with adsorptive properties can also increase the rate of removal of pollutants in water. For this purpose, materials with good adsorptive properties are combined with the semiconductor photocatalysts, and the respective advantages are brought into play. The low-concentration and highly toxic pollutants in wastewater are adsorbed on the surface of the photocatalysts, and then decomposed into H_2O, CO_2 and non-toxic inorganic acids.

Graphitic carbon nitride (g-C_3N_4), a metal-free polymeric semiconductor, has attracted extensive attention due to its good thermochemical stability, electronic properties, optical characteristics and suitable band gap (around 2.70 eV).[5–7] To date, the recent improvements with regards to g-C_3N_4 have been published in a large number of articles. For example, the different morphologies of g-C_3N_4, such as g-C_3N_4 quantum dots (QDs) and two-dimensionally ultrathin g-C_3N_4 nanosheets, were prepared successfully. In addition, g-C_3N_4 as a novel visible-light-driven photocatalyst has been reported for hydrogen evolution and pollutant degradation.[8–12] However, as a single-phase catalyst, g-C_3N_4 is restricted by its high recombination rate of photoinduced electron–hole pairs, leading to its poor quantum efficiency and low photocatalytic activity. In order to improve the photocatalytic performance of g-C_3N_4, numerous methods have been employed, such as doping of metal/nonmetal elements[13,14] and coupling with other semiconductors.[15,16] Hong *et al.* reported a novel direct solid-state Z-scheme V_2O_5/g-C_3N_4 heterojunction obtained by a facile *in situ* growth strategy for the first time. The photocatalytic performance was evaluated by the degradation of RhB and TC under visible light irradiation ($\lambda > 420$ nm).[17] Zhu *et al.* synthesized

---

[a] *Key Laboratory of Preparation and Application of Environmental Friendly Materials (Jilin Normal University), Ministry of Education, Changchun 130103, P. R. China. E-mail: guangboche@jlnu.edu.cn; Tel: +86-434-3295100*

[b] *School of Environmental Science and Engineering, Chang'an University, Xi'an 710054, P. R. China. E-mail: guanweisheng@263.net*

[c] *Institute of Green Chemistry & Chemical Technology, Jiangsu University, Zhenjiang 212013, P. R. China*

[d] *School of Materials Science and Engineering, Liaoning Technical University, Fuxin 123000, P. R. China*

† Electronic supplementary information (ESI) available. See DOI: 10.1039/c9ra08489d

a highly dispersed Ag/Fe_3O_4/g-C_3N_4 composite photocatalyst by means of the selective photo-deposition technique. It exhibited a significantly improved photocatalytic activity and stability for degrading TC, besides retaining the recyclable magnetic property.[18] Recent studies have shown that noble metal loading proved to be an effective way of increasing the photocatalytic activity. This is because the localized surface plasmon resonance (SPR) of a noble metal can enhance the localized electric fields by several distinct orders of magnitude at the noble metal/g-C_3N_4 photocatalyst interface. Noble metal nanoparticles can serve as antennae to capture photoinduced electrons from the conduction band (CB) of g-C_3N_4, thus decreasing the recombination of the electron–hole pairs and further improving the photocatalytic activity. Ag, as a low-cost and widely used noble metal, has been employed to synthesize composite photocatalysts, such as Ag@AgCl, Ag/AgX/GO and Ag/g-C_3N_4. However, there are still some disadvantages that restrict the application of Ag/g-C_3N_4 in environmental remediation,[19] particularly its low surface area.[20] Therefore, in order to further enlarge the adsorption capacity and improve the stability, it is necessary to modify Ag/g-C_3N_4 using porous materials.

As important porous materials, metal–organic frameworks (MOFs) have the advantages of adjustable pore size and pore surface, ultra-low density, ultra-high specific surface area, as well as insolubility in common solvents among other characteristics, compared with traditional pore materials, such as zeolites, mesoporous silica and activated carbon.[21–23] Consequently, much attention has been paid to the potential applications of MOFs in gas capture and storage, chemical separation, sensor devices, drug delivery and catalysis.[24–29] Wang *et al.* reported the synthesis of g-C_3N_4/Ti-benzenedicarboxylate (MIL-125(Ti)) heterostructure photocatalysts. By optimizing the compositions, an environment-friendly composite was found to show excellent photocatalytic activity towards RhB dye degradation under visible-light irradiation. The significantly reduced electron–hole recombination rate of photocatalysts was not only caused by the sufficient surface contact of g-C_3N_4 and MIL-125(Ti), but also induced by the synergic effect between g-C_3N_4 and MIL-125(Ti).[30] He *et al.* manifested the photocatalytic hydrogen production efficiency of CdS nanoparticles embedded on MIL-101 under visible-light irradiation, which was superior to that of bare CdS due to the large specific surface area, more active adsorption sites, photocatalytic reaction centers and good visible-light harvesting capability.[31] Liang *et al.* used a simple self-assembly strategy for increasing the interfacial contact to prepare MIL-53(Fe)-reduced graphene oxide nanocomposites.[32] Therefore, combining MOFs with semiconductor photocatalysts can improve the photocatalytic efficiency.

Herein, we report a facile process for the preparation of plasmonic AHC photocatalysts. First, the metal-free bulk g-C_3N_4 was synthesized by the thermal treatment of melamine. Second, we prepared HKUST-1/g-C_3N_4 composites by a facile *in situ* growth strategy. Finally, the AHC composite photocatalysts were successfully synthesized through a photo-deposition technique. In addition, the possible photocatalytic mechanism is tentatively proposed based on the active species trapping and ESR experiments. Furthermore, the stability of AHC composite photocatalyst was tested by the circulation experiments.

Experimental section

Materials and methods

$AgNO_3$, $Cu(NO_3)_2$, trimesinic acid (H_3BTC), melamine, ethanol, acetic acid, polyethylene glycol 800 (PEG 800), triethanolamine (TEOA), isopropanol (IPA), and 5,5-dimethyl-1-pyrroline N-oxide (DMPO) were analytical grade agents and purchased from Aladdin (China). RhB was analytically pure and used without further purification. All of the phase compositions and crystal structures of the prepared samples were determined by the powder X-ray diffraction (XRD) method using Cu Kα radiation ($\lambda = 1.54178$ Å) (D/MAX-2500 diffractometer, Rigaku, Japan) with a Cu Kα radiation source ($k = 1.54056$) over the 2θ range of 5–90° at a scanning rate of 10° min^{-1}. The morphologies and structure details of the as-prepared samples were obtained using scanning electron microscopy (SEM, JSM-6510) and transmission electron microscopy (TEM, JEM-2100F). X-ray photoelectron spectroscopy (XPS) maps were obtained by a Thermo ESCALAB 250X (America) electron spectrometer using a 150 W Al Kα X-ray source. The specific surface area of these samples was determined from the nitrogen absorption–desorption data and Brunauer–Emmett–Teller (BET) measurements (ASAP2020, Micromeritics, USA). The UV-vis diffused reflectance spectra (DRS) of the samples were obtained from a UV-vis spectrophotometer (UV-2450, Shimadzu, Japan); $BaSO_4$ was used as a reflectance standard. The photoluminescence (PL) spectra for the solid samples were obtained on a F4500 (Hitachi, Japan) photoluminescence detector. The photocurrent and electrochemical impedance spectroscopy (EIS) measurements were conducted using a CHI660C (Chenhua Instruments Co. Shanghai China) electrochemical workstation. The electron spin resonance (ESR) analysis was conducted with a Bruker EPR A 300-10/12 spectrometer.

Photocatalysts preparation

Synthesis of g-C_3N_4 sheets. The metal-free bulk g-C_3N_4 was synthesized by the thermal treatment of melamine, according to a previous report.[33] Typically, 10 g melamine was put into a 50 mL alumina crucible with a cover, and then heated in a muffle furnace at a rate of 2.3 °C min^{-1} and kept for 4.0 h at 550 °C. After being cooled to room temperature, the resulting products were collected and milled into powder in an agate mortar for further use.

Synthesis of AHC. The HKUST-1/g-C_3N_4 composites were synthesized according to a modified method.[34] First, a certain amount of g-C_3N_4 was dispersed into ethanol with the aid of ultrasonication. Then, H_3BTC (0.1 mmol) was added into a mixture of g-C_3N_4/ethanol (30 mL) and sonicated for 30 min to afford a homogeneous solution. Second, copper acetate ($Cu(OAc)_2 \cdot H_2O$; 0.15 mmol) was dissolved in acetic acid solution (HAc: 3.0 mL; H_2O: 30 mL) to form another solution. Subsequently, the solutions obtained in the first step and the second step were mixed and stirred for an hour at high speed.

The products were collected by centrifugation at 11 000 rpm for 3.0 min, washed with ethanol several times, and finally dried in an oven at 60 °C for 10 h.

A certain amount of the as-prepared HKUST-1/g-C_3N_4 was mixed with 200 mL of deionized water by ultrasonication for 30 min. Then, 1.0 mL of 5% polyethylene glycol (PEG) 800 solution was added and the dispersion was stirred for another 10 min.[35,36] For deposition of silver on the surface of HKUST-1/g-C_3N_4, a photo-deposition technique was applied as follows. Initially, 5.0 mL of $AgNO_3$ solution (0.015 mol L^{-1}) was added to the dispersion. Then, the suspension was transferred to a water-cooled reactor (250 mL) and irradiated under a PLS-SXE300 Xe lamp with 250 W illumination intensity for 60 min. The theoretical value of the Ag loading amount was 4.0 wt%. Subsequently, 5% AHC, 6% AHC, and 7% AHC were synthesized.

Photocatalytic experiments

The photocatalytic activities of the as-prepared samples were investigated by the degradation of RhB under visible light irradiation. The typical photocatalytic experiment was performed in a Pyrex reactor with refluxed water at room temperature and illuminated using a 250 W xenon lamp with a 420 nm cut off filter. In detail, 50 mg of the powered samples was dispersed in the 100 mL of 0.5 mg L^{-1} pollutant aqueous solutions. In order to ensure the adsorption equilibrium, the suspension was continuously stirred for 45 min in the dark before irradiation. The concentration changes of the pollutant aqueous solutions were monitored by measuring the UV-vis absorption of the suspensions at 15 min intervals. During irradiation, 5.0 mL of the suspension was taken out and centrifuged (10 000 rpm, 2.0 min) to remove the photocatalyst before measurements. Then, the supernatant was monitored by a UV-vis spectrophotometer at the characteristic absorption of RhB at 553 nm.

Photoelectrochemical measurements

The photocurrent and electrochemical impedance spectra tests were performed using a CHI660C electrochemical workstation in a standard three-electrode configuration, with the as-prepared samples as the working electrodes, a Pt foil as the counter electrode and an Ag/AgCl electrode as a reference electrode. A 0.5 mol L^{-1} Na_2SO_4 aqueous solution was used as the electrolyte. The working electrodes were prepared as the follows: 0.3 g of each sample, 0.03 mL oleic acid and 0.01 g of polyvinyl pyrrolidone (PVP) were dissolved in 3.0 mL of ethanol to form a suspension, which was then spin coated onto a 15 mm × 20 mm indium tin oxide (ITO) conducting glass electrode by using a drop-casting method and annealed at 500 °C in air for 2.0 h. The visible light source was provided by a 300 W xenon lamp with a 420 nm cut off filter was used to filter out UV light ($\lambda < 420$ nm).

Active species trapping and ESR experiments

It is well known that the holes (h^+), superoxide radical ($\cdot O_2^-$) and hydroxyl radicals ($\cdot OH$) were the major reactive species for the photocatalytic oxidation. In the active species trapping experiments, 1.0 mM TEOA and 1.0 mM IPA were respectively employed as the scavengers for h^+ and $\cdot OH$. The method is similar to the former photocatalytic activity test. Furthermore, the ESR technique was further used to discover the existence of $\cdot O_2^-$ and $\cdot OH$ radicals in the photocatalytic reaction system under visible light ($\lambda > 420$ nm). The samples for ESR measurements were prepared as follows: 10 mg of each of the samples was dissolved in 0.5 mL methanol (DMPO–$\cdot O_2^-$) or 0.5 mL deionized water (DMPO–$\cdot$OH) and then, 45 μL DMPO was added to the solution, followed by ultrasonic dispersion for 5.0 min.

Results and discussion

Structure and morphology analysis

The XRD patterns of the as-prepared g-C_3N_4, 4% AHC, 5% AHC, 6% AHC, 7% AHC, HKUST-1 and Ag (PDF#87-0718) are shown in Fig. 1. As can be seen, pure g-C_3N_4 shows one diffraction peak ascribed to the (100) plane at about $2\theta = 13.1°$, corresponding to the characteristic interlayer structural packing. Another diffraction peak ascribed to the (002) plane at 27.2° corresponds to the interplanar stacking peaks of the aromatic systems.[37,38] Compared with pure g-C_3N_4, the 4% AHC, 5% AHC, 6% AHC and 7% AHC samples exhibit two additional peaks at 38.2° and 44.4°, which are indexed to the (111) and (200) planes of Ag, respectively. Such observations indicate that the Ag NPs were successfully loaded on g-C_3N_4 after irradiation.[39] Nevertheless, the diffraction peaks of HKUST-1 were not detected in the samples of AHC, which may be due to its low loading content and high dispersity.

The morphologies and microstructures of g-C_3N_4 and 5% AHC composite photocatalyst were further investigated by TEM and SEM (Fig. 2). As shown in Fig. 2(a), it could be observed that g-C_3N_4 displays two dimensional and overlapped lamellar structures, whereas as shown in Fig. 2(b), for 5% AHC, irregular Ag NPs and HKUST-1 particles, which covered with bits of g-

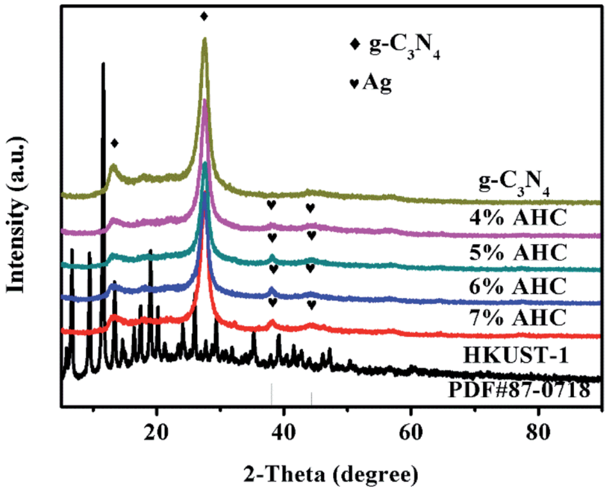

Fig. 1 XRD patterns of the as-prepared g-C_3N_4, 4% AHC, 5% AHC, 6% AHC, 7% AHC and HKUST-1 composites.

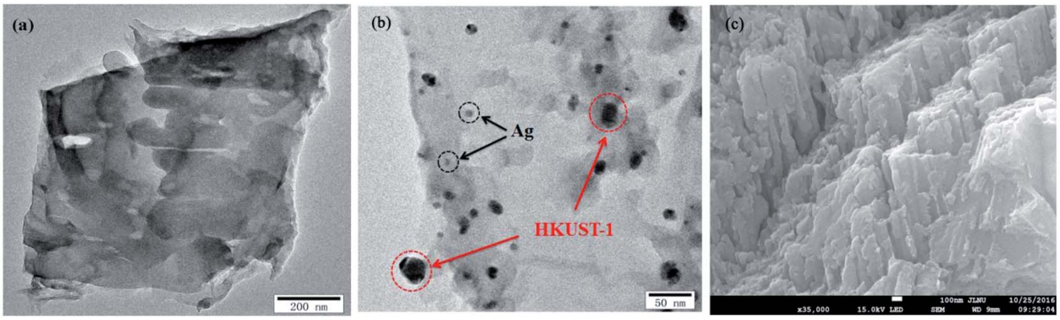

Fig. 2 TEM images of (a) pure g-C_3N_4; (b) 5% AHC; (c) SEM image of 5% AHC.

C_3N_4 nanosheets, were found to be embedded in the wrinkling g-C_3N_4 lamellar structure. The SEM image of 5% AHC (Fig. 2(c)) and its EDS elemental mappings (Fig. S1†) further confirm that the 5% AHC composite photocatalyst was composed of Ag, Cu, C, N and O elements. Thus, the composite obtained by combining Ag, HKUST-1 and g-C_3N_4 was successfully fabricated.

Herein, based on the above experimental results, it could be demonstrated that the AHC composite photocatalysts were successfully synthesized, which were expected to facilitate the transfer of photo-generated charge carriers.

Chemical states analysis

XPS spectra were employed to analyze the detailed chemical status of the samples. The spectra were recorded to analyze the surface chemical compositions of g-C_3N_4, HKUST-1 and 5% AHC composite photocatalyst. The XPS survey spectra of g-C_3N_4, HKUST-1 and 5% AHC samples are shown in Fig. 3(a). The spectra indicated that C and N exist on the surface of g-C_3N_4, Cu, C and O exist on the surface of HKUST-1, and Ag, C, N and O exist in 5% AHC. The doublet peaks of Ag $3d_{5/2}$ and Ag $3d_{3/2}$ were located at about 366.08 eV and 372 eV, respectively, which were very close to the binding energy values of Ag (Fig. 3(b)).[40] The Cu 2p XPS spectra for HKUST-1 and 5% AHC are shown in Fig. 3(c). For HKUST-1, the peaks of Cu $2p_{3/2}$ and Cu $2p_{1/2}$ located at 934 eV and 953.6 eV, respectively. However, when HKUST-1 combined with g-C_3N_4, the Cu $2p_{3/2}$ peak of 5% AHC displayed a slight shift. Furthermore, the well-known ''shake-up satellite bands'' (at the 937–946 eV regions) were clearly observed, which was indicative of the paramagnetic chemical state of Cu^{2+}.[41] Correspondingly, for HKUST-1, the peaks of O 1s are located at 530.5 eV and 531.5 eV, respectively. However, one of the O 1s peaks of 5% AHC also exhibited a slight shift to the lower binding energy at about 530.4 eV (Fig. 3(d)). Fig. 3(e)

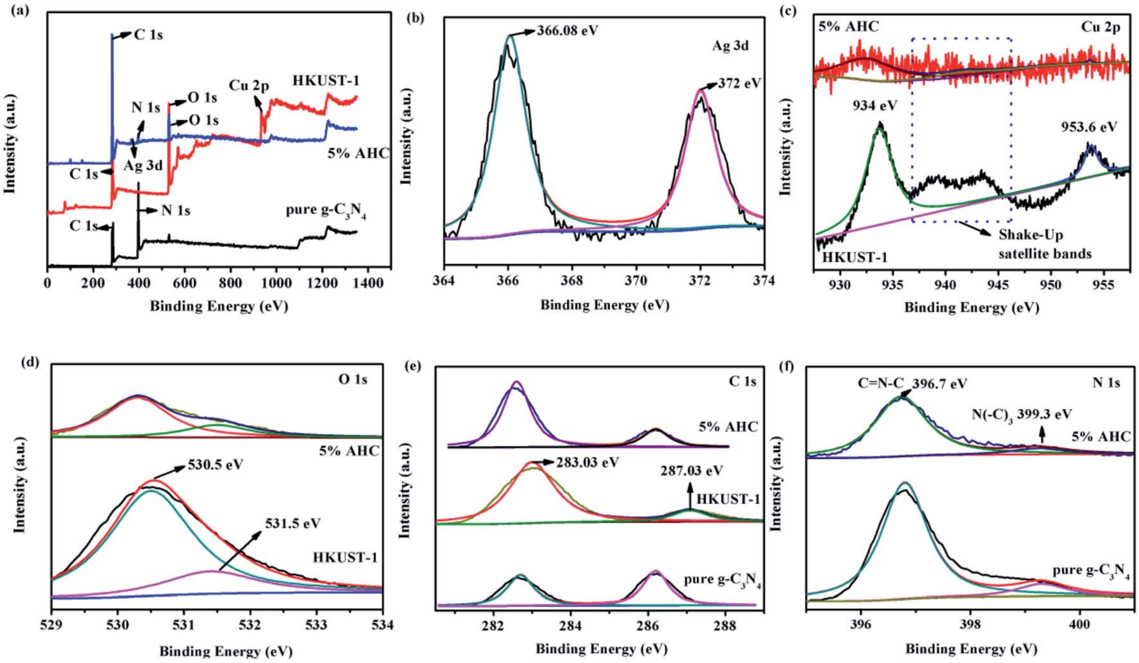

Fig. 3 XPS spectra of pure g-C_3N_4, HKUST-1 and 5% AHC samples: (a) survey spectrum; (b) Ag 3d; (c) Cu 2p; (d) O 1s; (e) C 1s and (f) N 1s.

displays two strong peaks at 283.03 eV and 287.03 eV, which were assigned to C 1s, which should originate from HKUST-1. The binding energy of C 1s in the 5% AHC composite photocatalyst also exhibited a slight shift to the low energy region compared to that of HKUST-1. These binding energy shifts in the spectra could be attributed to the presence of strong interactions between g-C_3N_4 and HKUST-1. In the N 1s spectrum (Fig. 3(f)), two peaks at 396.7 eV and 399.3 eV are separately ascribed to sp^2 N bonded to two carbon atoms (C=N–C) and tertiary nitrogen (N–$(C)_3$).[42,43] The XPS results validate the coexistence of Ag, g-C_3N_4 and HKUST-1 in the 5% AHC composite photocatalyst. In addition, it is also concluded that there are strong interfacial interactions between g-C_3N_4 and HKUST-1, which could facilitate the rapid transfer of photoinduced charge and improve the photocatalytic performance of 5% AHC.

Specific surface area and optical properties

The N_2 adsorption–desorption isotherms of pure g-C_3N_4 and 5% AHC are shown in Fig. 4. It can be seen that the isotherms are similar and all of them are classical type IV, suggesting the presence of abundant mesopores and macropores. The BET surface area of pure g-C_3N_4 was found to be 10.4 $m^2\ g^{-1}$, while that of 5% AHC was 27.4 $m^2\ g^{-1}$, which was higher than that of pure g-C_3N_4. Correspondingly, the total pore volume of 5% AHC was 0.12 $cm^3\ g^{-1}$, which was higher than that of pure g-C_3N_4 (0.08 $cm^3\ g^{-1}$). The pore size distribution (PSD) of 5% AHC was calculated *via* nonlocal density functional theory (NLDFT) (the inset in Fig. 4). The 5% AHC composite photocatalyst exhibits a dominant pore width of about 20 nm and several smaller pores in the pore-size range of 60–100 nm. The PSD curves agree with the shape of the nitrogen isotherms (Fig. 4) and suggest that the polymers are predominantly mesoporous and macropores.

The optical properties of the as-prepared g-C_3N_4, HKUST-1, 5% Ag/g-C_3N_4 (the method of synthesis was in the ESI), and 5% AHC composite photocatalyst were measured *via* the UV-vis DRS technique. As shown in Fig. 5(a), it is clear that pure g-C_3N_4 shows absorption wavelengths from UV to visible range up to 460 nm, and its band gap is around 2.70 eV, which agrees well with the previous reports.[44,45] Compared with that of pure g-C_3N_4, the absorption edge of the 5% Ag/g-C_3N_4 composite photocatalyst shows a systematic slight red shift. This may be attributed to the surface plasmon resonance (SPR) effect of Ag species.[46] Furthermore, HKUST-1 displays an absorption band lower than about 460 nm, resulting in a low visible light utilization efficiency. However, as the wavelength increases, the response of HKUST-1 to the visible light becomes stronger. Therefore, the 5% AHC composite photocatalyst has a strong absorption under visible light irradiation, suggesting that it can efficiently utilize the visible light for the degradation of organic dyes pollutants. Furthermore, in order to confirm the relative band gap position of the samples, the band gap energy (E_g) of sample was calculated by the following formula based on the DRS results (1):

$$\alpha h\nu = A(h\nu - E_g)^{n/2} \qquad (1)$$

where α is the absorption coefficient, ν is the optical frequency, E_g is the band gap energy, and A is a constant. As shown in Fig. 5(b), the band gap energy of g-C_3N_4, HKUST-1, 5% Ag/g-C_3N_4 and 5% AHC can be estimated to be 2.71 eV, 2.89 eV, 2.63 eV and 2.11 eV, respectively. Similarly, the band gap energy of g-C_3N_4, HKUST-1, 5% Ag/g-C_3N_4 and 5% AHC can also be inferred from a plot of $(\alpha h\nu)^2$ *versus* energy ($h\nu$).

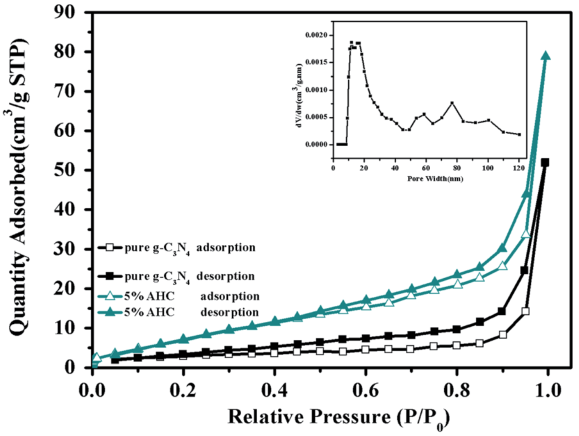

Fig. 4 N_2 adsorption–desorption isotherms of the as-prepared pure g-C_3N_4 and 5% AHC samples (closed symbols: desorption; open symbols: adsorption; inset: pore size of 5% AHC).

The transfer and recombination processes of electron–hole pairs in the interfaces of the composite photocatalysts are one of most important factors that affect the photocatalysis activity. PL analysis was used to estimate the photoinduced charge carrier separation and transfer ability of the as-prepared samples. It is well acknowledged that the higher PL intensity indicates the fast recombination of the charge carriers, resulting in lower photocatalytic activity. Fig. 6 presents the PL spectra of g-C_3N_4 and AHC with an excitation wavelength of 325 nm.[47] Pure g-C_3N_4 has a strong peak at around 466 nm in the PL spectrum, which can be attributed to the band gap recombination of electron–hole pairs.[48] However, the quenching phenomenon exists in the PL spectrum of AHC, which is related to good electrical conductivity and induced SPR effect of the Ag species. Therefore, AHC inhibits a more effective recombination of photogenerated charge carriers to improve photocatalytic activity. Moreover, the PL intensity of the 5% AHC composite photocatalyst possessed the lowest PL intensity, suggesting its high photocatalytic activity.

Photocatalytic activity

The photocatalytic activities of the as-prepared samples were evaluated by the degradation of RhB under visible light irradiation ($\lambda > 420$ nm). As shown in Fig. 7(a), the concentration of RhB could reach adsorption–desorption equilibrium after reaction under dark for 45 min. It can be seen that the adsorption of 5% AHC was significantly better than that of pure g-C_3N_4 and 5% Ag/g-C_3N_4. Hence, more RhB molecules can be adsorbed, which was beneficial for improving their visible light activities.

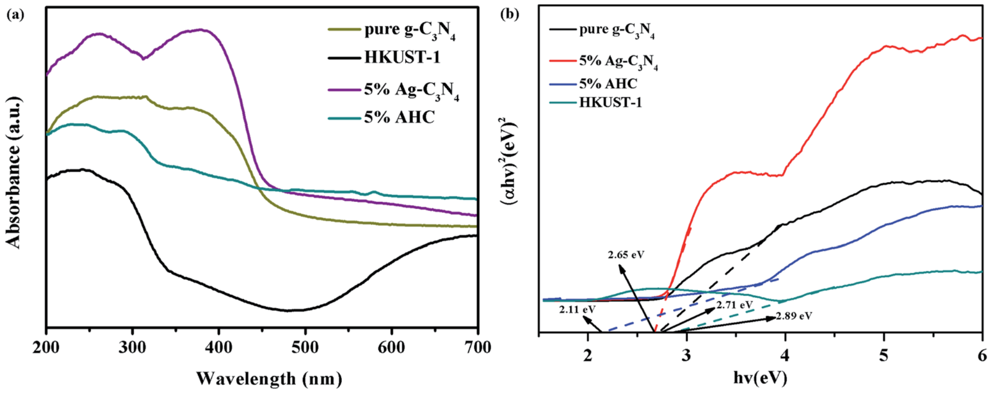

Fig. 5 (a) UV-vis diffuse reflectance spectra of pure g-C_3N_4, HKUST-1 and 5% AHC; (b) the plots of $(\alpha h\nu)^2$ *versus hv* for the band gap energies of pure g-C_3N_4, HKUST-1 and 5% AHC.

The photocatalytic activities of the AHC composite photocatalysts with different Ag contents as well as the blank, pure g-C_3N_4 and 5% Ag/g-C_3N_4 were tested under visible light irradiation. As shown in Fig. 7(b) and (c), the blank test without a catalyst reveals that the photolysis of RhB occurs very slowly, which can be neglected. As shown in Fig. 7(b), when the content of Ag species increases to 5.0 wt%, the photocatalytic activity of AHC is optimal and the degradation rate of RhB reaches 87.4% while undergoing a photocatalytic reaction for 90 min. In particular, with respect to the introduction of Ag species, Ag NPs deposited on the surface of HKUST-1/g-C_3N_4 not only induce a plasmon resonance effect to widen light absorption ability, but also export photogenerated electrons on the HKUST-1/g-C_3N_4, which more efficiently improve the separation ability of the electron–hole pairs, thus resulting in the higher photocatalytic activity. However, the excess Ag species will lead to the reduction of photocatalytic activity owing to the shielding effect that weakens light harvesting ability of AHC. Fig. 7(c) indicates that the pure g-C_3N_4 sample exhibits low photocatalytic performance for the degradation of RhB under visible light. Furthermore, using 5% Ag/g-C_3N_4, 70% RhB was degraded. However, the as-synthesized 5% AHC composite photocatalyst can efficiently enhance the photocatalytic activity compared with the g-C_3N_4 and 5% Ag/g-C_3N_4. This is mainly because HKUST-1 not only has good adsorption performance, but can also be used as a medium for the rapid transfer of photogenerated charges.

At the same time, the kinetic behavior of photocatalytic degradation using the composite photocatalysts was further investigated, and the results are shown in Fig. 7(d) and (e); all of the plots fit well with the pseudo-first-order correlation:

$$\ln(C_0/C) = kt$$

where C is the concentration of RhB remaining in the solution at irradiation time t, C_0 is the initial concentration at $t = 0$, and k is the apparent rate constant for degradation. The order of the RhB degradation rate for the as-prepared photocatalysts was 5% AHC (0.021 min^{-1}) > 4% AHC (0.016 min^{-1}) > 6% AHC (0.015 min^{-1}) > 5% Ag/g-C_3N_4 (0.014 min^{-1}) > 7% AHC (0.012 min^{-1}) > pure g-C_3N_4 (0.007 min^{-1}) > blank (0.00095 min^{-1}).

Furthermore, for the photocatalysts, the durability and stability are also crucially important for their practical applications. After each cycling test, the samples were collected and washed with distilled water and absolute ethanol three times and then, the as-obtained samples were dried in vacuum at 80 °C for 12 h for further cycling. The recycling capability of 5% AHC was verified by performing a four-run test for the degradation of RhB. As shown in Fig. 8, no significant inactivation of the photocatalysts was observed, revealing that the 5% AHC composite photocatalyst possesses high stability for its practical application. Moreover, in order to further testify the reusability and stability of the catalysts, the XRD pattern of the 5% AHC composite photocatalyst after 4th run was obtained (Fig. S2†). There was no apparent change in intensity after the photocatalytic reaction, which once again proved the stability of the catalyst.

Photocatalytic activity photocurrents and EIS analyses

To further understand the separation and recombination of electron–hole pairs in the composite photocatalysts, the photocurrents over all the as-prepared samples have been investigated. Generally, the corresponding relationship was that

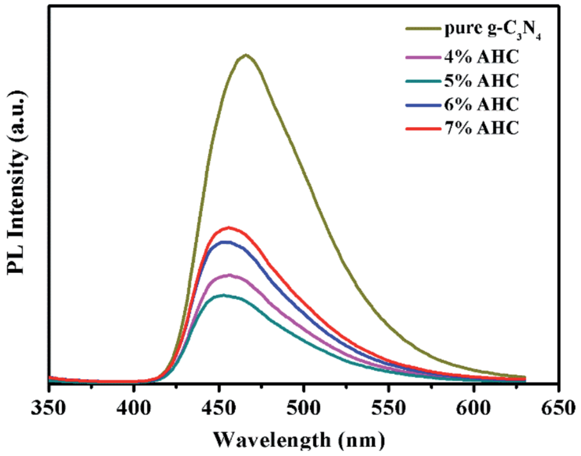

Fig. 6 Photoluminescence (PL) spectra of pure g-C_3N_4 and AHC.

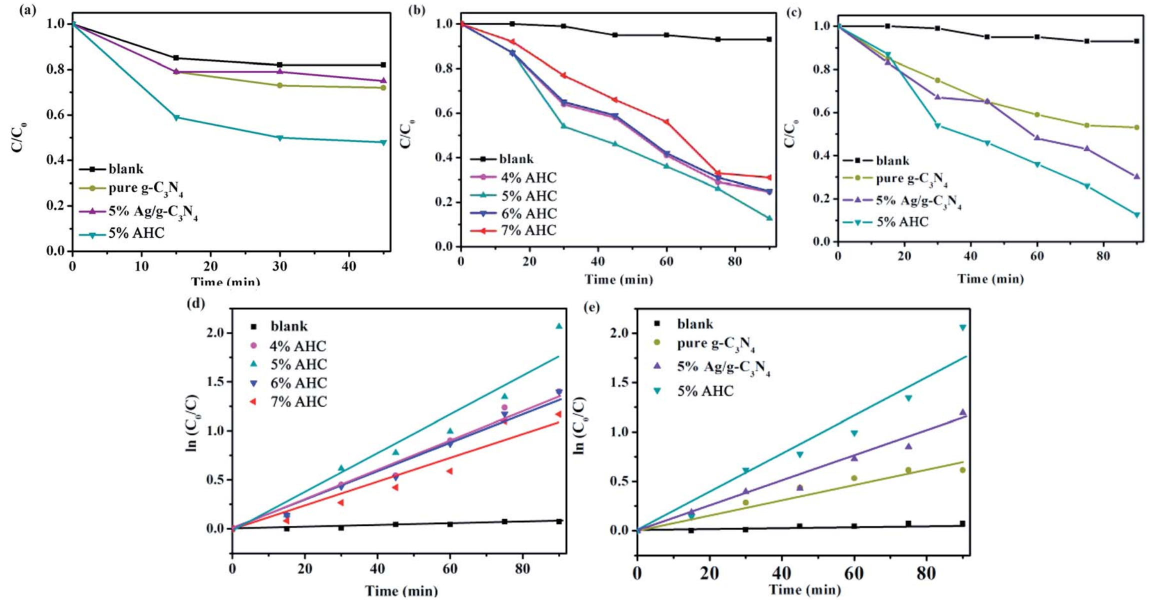

Fig. 7 (a) The dark adsorption–desorption equilibrium of RhB in catalysts; (b and c) the photocatalytic activities of as-prepared samples for RhB degradation under visible-light (λ > 420 nm); (d and e) the first-kinetic of the photocatalytic degradation of RhB.

the higher photocurrent implies the higher electron–hole separation efficiency, thus leading to higher photocatalytic activity.[49] It can be clearly observed from Fig. 9(a) that rapid and stable photocurrent responses are detected in all the as-prepared samples as electrodes under visible light illumination. Clearly, the 5% AHC composite photocatalyst presents the higher photocurrent response intensity than other composites, which indicates that it has the lowest electron–hole recombination rate. This conclusion can be confirmed by PL measurements. In addition, the separation of photogenerated charge carriers can be illustrated by the EIS.[50,51] EIS was performed to explore the process of their charge transfer resistance. The radius of the arc in the EIS Nyquist plot represented the charge transfer rate occurring at the contact interface between the working electrode and electrolyte solution. The smaller radius of the Nyquist arc indicates lower charge transfer resistance.[52] As shown in Fig. 9(b), all the AHC samples feature significantly smaller radius than pure g-C_3N_4. All the above results indicated that introducing Ag had a positive effect on the separation and transfer of photogenerated charge carriers. Moreover, the arc radius of the 5% AHC composite photocatalyst was the smallest, demonstrating the fast interfacial charge transfer property of 5% AHC.

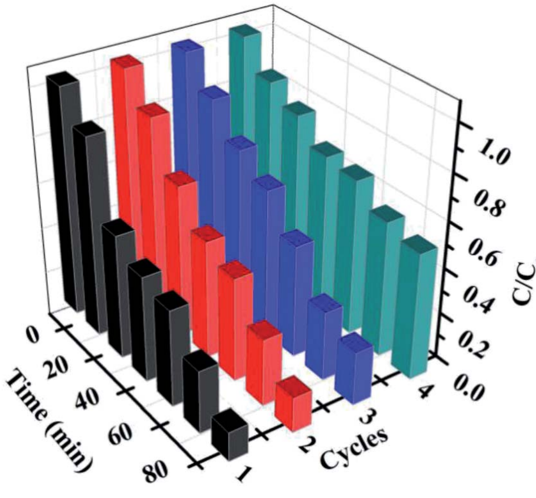

Fig. 8 The four reaction cycles of 5% AHC photocatalyst for the degradation of RhB.

HPLC-MS spectra analysis

In order to investigate the intermediates and pathways in depth during the degradation of RhB, HPLC-MS experiments were performed. As shown in Fig. 10, RhB was depicted with a fragment ion at m/z 443, which is in good consistency with deprotonated RhB. As shown in Fig. 11, on progression of the reaction, RhB is resolved into small molecules with $m/z = 443$, $m/z = 415$, $m/z = 387$, and $m/z = 274$. The rest of the fragments may be derived from other complex intermediate products. Finally, with the progress of photocatalytic reaction, the intermediate products would be degraded to CO_2, H_2O, and NH_4^+ and some other small inorganic molecular materials.

Photocatalytic mechanism

In order to explore the photocatalytic mechanism of RhB, different active species trapping experiments were conducted. The interaction between the capturer and photocatalyst played a dominant role in impacting the degradation efficiency of organic molecules.[18] Therefore, a series of radical trapping experiments were performed using TEOA (a quencher of h^+) and IPA (a quencher of $\cdot$OH) over the 5% AHC composite

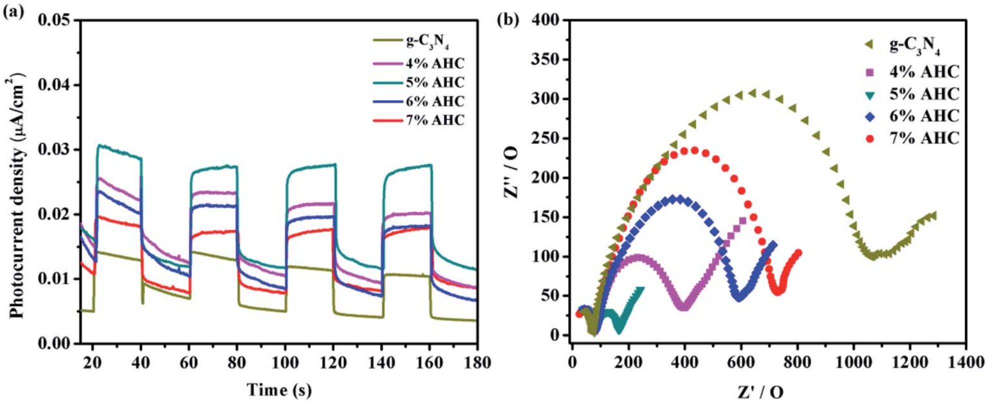

Fig. 9 (a) Transient photocurrent response of the as-prepared samples; (b) electrochemical impedance spectroscopy of as-prepared samples.

photocatalyst.[53–55] As shown in Fig. 12 and S3,† for the 5% AHC sample (87.4%), it can be seen that when TEOA was added, the photocatalytic degradation rate significantly decreased (8%), indicating that h^+ was the predominant active species. When IPA was added into reaction solution, the degradation rate of RhB was also inhibited (51%), suggesting that ·OH also played an important role in the photocatalytic degradation process.

The ESR technique was further used to detect the presence of ·OH and $\cdot O_2^-$ radicals in the 5% AHC photocatalytic reaction systems under visible light. As can be seen from Fig. 11a and b, no ESR signals were observed when the reaction was performed in the dark. As expected, for the 5% AHC sample, the four characteristic peaks of the DMPO–·OH adducts were observed (Fig. 13(a)), indicating that the ·OH radicals were produced in 5% AHC reaction systems. In addition, weak characteristic peaks of DMPO–$\cdot O_2^-$ adducts were observed (Fig. 13(b)), indicating that $\cdot O_2^-$ radicals were produced in the 5% AHC reaction system. However, the number of $\cdot O_2^-$ radicals were less than the number of ·OH radicals.

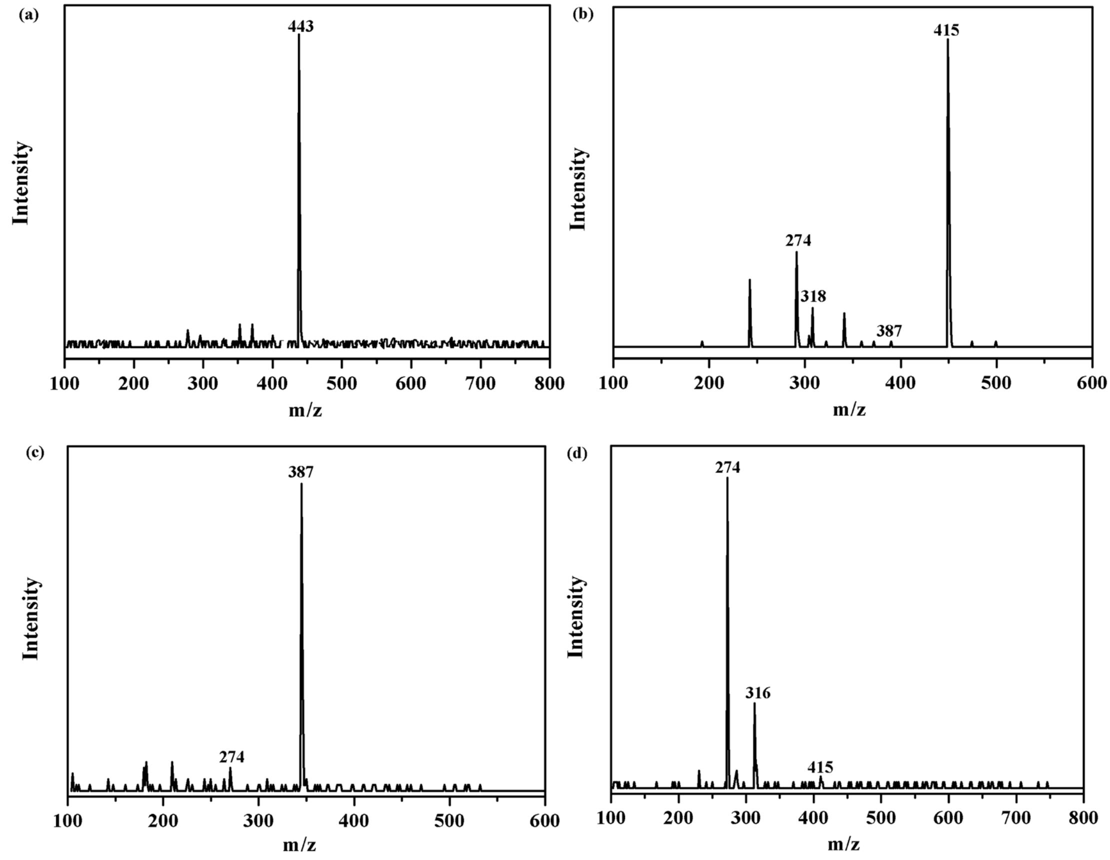

Fig. 10 *m/z* of degraded RhB over the 5% AHC composite photocatalyst: (a) the initial RhB solution; (b) degradation of RhB after 30 min; (c) degradation of RhB after 60 min; (d) degradation of RhB after 90 min.

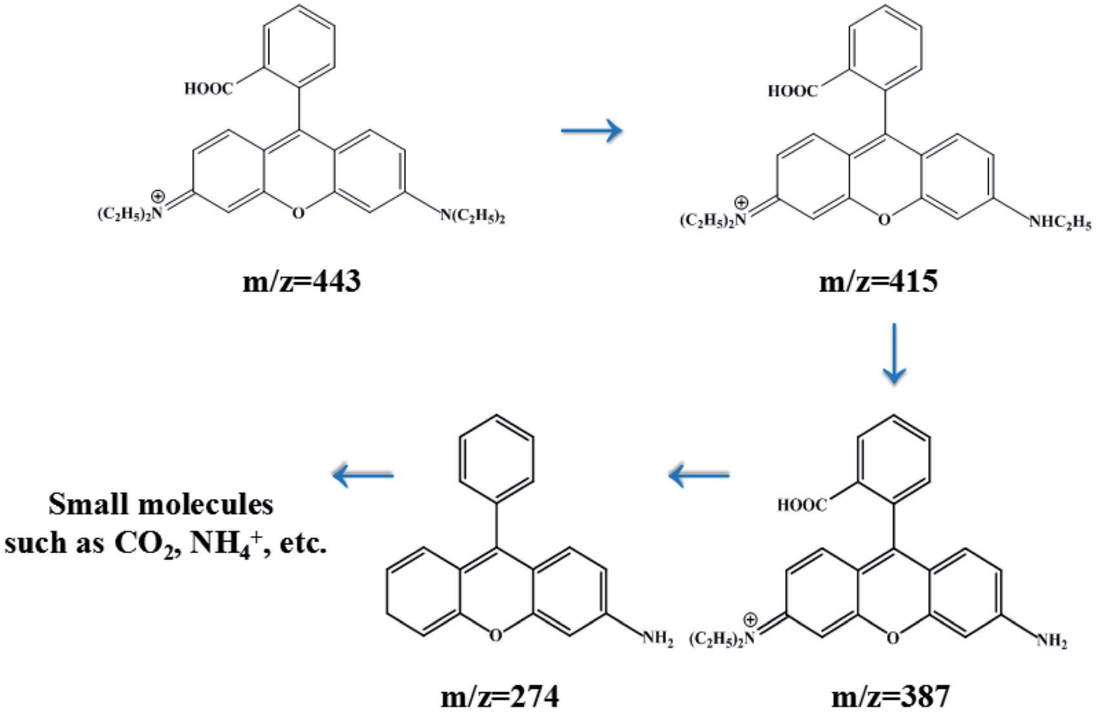

Fig. 11 Degradation process of RhB with its intermediate products over 5% AHC.

Thus, the influence order of the activated species in the process of RhB photodegradation was $h^+ > \cdot OH > \cdot O_2^-$. Therefore, according to the above results of the active species trapping experiments and ESR analysis, we can make a conclusion that the h^+ and $\cdot OH$ play major roles and $\cdot O_2^-$ plays a secondary role in the 5% AHC photocatalytic degradation reaction.

Combined with the above discussion, the possible photocatalytic mechanism for the degradation of RhB with 5% AHC composite photocatalyst is proposed, as shown in Fig. 14. First, under visible-light irradiation, $g\text{-}C_3N_4$ can be excited and photoinduced electrons and holes are generated (eqn (2)). Electrons are rapidly transferred from the $g\text{-}C_3N_4$ conduction band to the HKUST-1 surface. Due to this, the organic bridging ligands of HKUST-1 can serve as antennae to harvest visible light and then effectively transfer the energy to the inorganic copper-oxygen cluster parts. Subsequently, the photogenerated electrons on HKUST-1 rapidly migrate to the Ag surface. Some of the photoelectrons on the $g\text{-}C_3N_4$ conduction band indirectly transfer to Ag NPs *via* HKUST-1 and serve as terminal electron acceptors, thus prolonging the photogenerated electron lifetime and facilitating the charge separation in the entire photocatalytic system. This result has been confirmed by the PL spectra, photocurrent test and EIS analyses. Second, the photogenerated electrons react with O_2 absorbed on the surface of Ag NPs to produce the active species $\cdot O_2^-$ (eqn (3)) because the E_{CB} value of $g\text{-}C_3N_4$ (−1.13 eV) was more negative than the potential of $O_2/\cdot O_2^-$ (−0.33 eV). Then, $\cdot O_2^-$ may also react with H^+ to further produce $\cdot OH$ (eqn (4)–(7)) based on the results of active species trapping and ESR analysis. Thus, both $\cdot O_2^-$ and $\cdot OH$ can oxidize RhB (eqn (8) and (9)). Moreover, the E_{VB} value of $g\text{-}C_3N_4$ (+1.57 eV) was lower than the standard redox potential of $\cdot OH/OH^-$ (+1.99 eV), and photogenerated holes (h^+) left on the VB of $g\text{-}C_3N_4$ could not react with H_2O or OH^- to generate the active oxidative species $\cdot OH$. Hence, h^+ on the VB of $g\text{-}C_3N_4$ would be consumed by directly decomposing RhB (eqn (10)).[56,57] The major routes of the photocatalytic degradation of RhB under visible-light irradiation are proposed as follows:

$$g\text{-}C_3N_4 + h\nu \rightarrow g\text{-}C_3N_4\,(e^- + h^+) \quad (2)$$

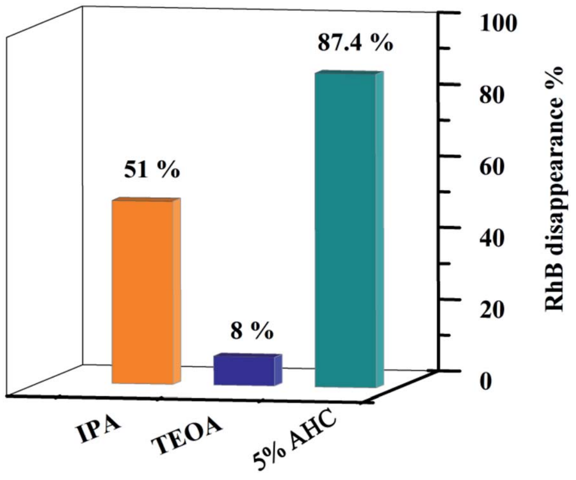

Fig. 12 Photodegradation rates of RhB over 5% AHC in the present of different scavengers.

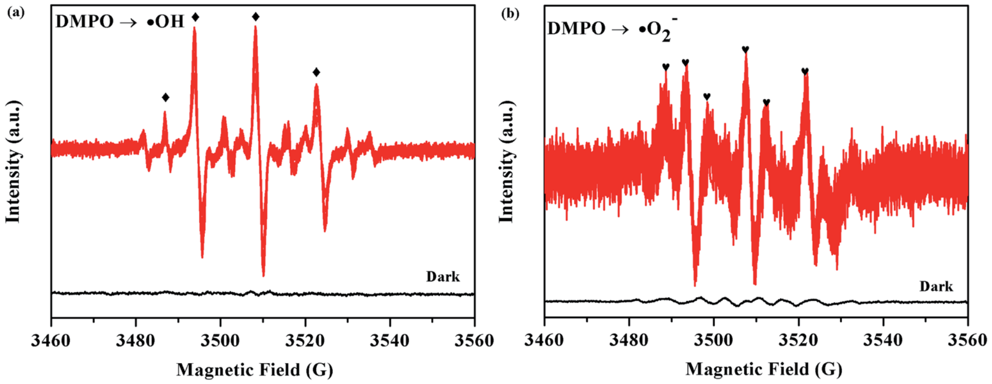

Fig. 13 ESR spectra of the 5% AHC sample for (a) DMPO–·OH and (b) DMPO–$\cdot O_2^-$.

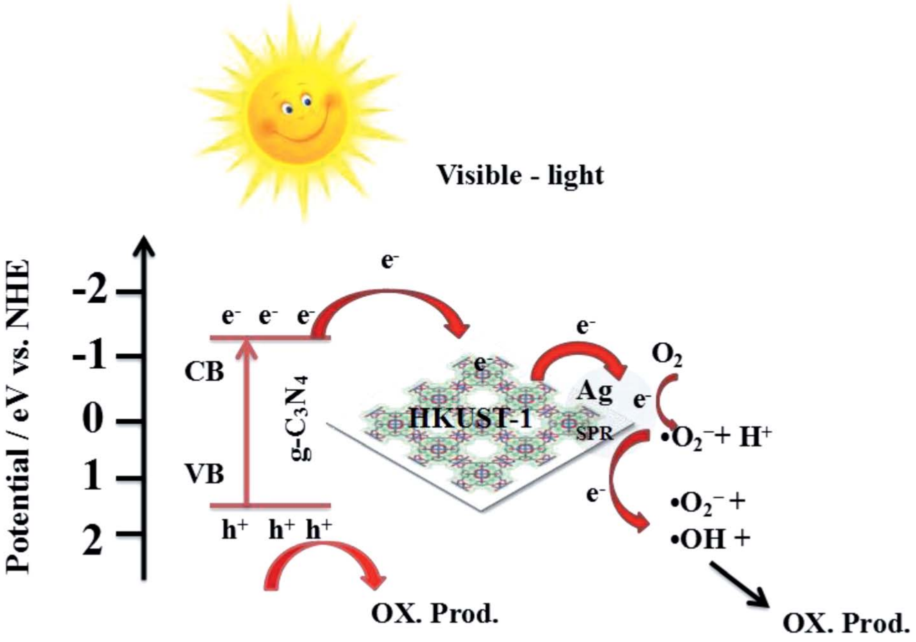

Fig. 14 Possible mechanism for the photo-induced charge transfer route of 5% AHC photocatalyst.

$$O_2 + e^- \rightarrow \cdot O_2^- \tag{3}$$

$$\cdot O_2^- + 2H^+ + e^- \rightarrow H_2O_2 \tag{4}$$

$$H_2O_2 + e^- \rightarrow \cdot OH + OH^- \tag{5}$$

$$OH^- + h^+ \rightarrow \cdot OH \tag{6}$$

$$H_2O + h^+ \rightarrow \cdot OH + H^+ \tag{7}$$

$$\cdot O_2^- + \text{RhB} \rightarrow \text{OX. prod.} \tag{8}$$

$$\cdot OH + \text{RhB} \rightarrow \text{OX. prod.} \tag{9}$$

$$h^+ + \text{RhB} \rightarrow \text{OX. prod.} \tag{10}$$

Conclusions

In summary, *in situ* growth strategy and photo-deposition technique were utilized to fabricate the 5% AHC composite photocatalyst. The 5% AHC composite photocatalyst exhibited superior photocatalytic performance in the degradation of RhB compared with pure g-C_3N_4 and other percentages of AHC. The enhanced photocatalytic activity under visible light irradiation can be ascribed to the adsorption and superior electron transport property of HKUST-1 and surface SPR of Ag, which greatly promoted the efficient separation of the photoexcited electron–hole pairs as well as depressed the recombination of the charge carriers. Finally, the present study provides the feasibility of designing new composite photocatalysts *via* a facile synthetic method and gives a new direction to design other high-efficiency composite semiconductor photocatalysts for practical applications.

Conflicts of interest

There are no conflicts to declare.

Acknowledgements

This study was supported by the National Natural Science Foundation (No. 21905107, 21902060, 21576112, 21607051), Natural Science Foundation Project of Jilin Province (20180623042TC, 20180101181JC, 20150623024TC-19, 20170520147JH), the Project of Human Resources and Social Security Department of Jilin Province (2017956), and the Project of Education Department of Jilin Province (JJKH20180775KJ, JJKH20191009KJ).

References

1 S. Debén, J. A. Fernández, A. Carballeira and J. R. Aboal, *Environ. Pollut.*, 2016, **210**, 315–322.
2 H. K. Yan, N. Wang, T. L. Yu, Q. Fu and C. Liang, *Mar. Pollut. Bull.*, 2013, **71**, 29–40.
3 A. Álvarez-Martín, M. S. Rodríguez-Cruz, M. S. Andrades and M. J. Sánchez-Martín, *Environ. Sci. Pollut. Res.*, 2016, **23**, 9192–9230.
4 H. Li, Y. Jing, X. L. Ma, T. Y. Liu, L. F. Yang, F. Liu, S. Yin, Y. Z. Wei and Y. H. Wang, *RSC Adv.*, 2017, **7**, 8688–8693.
5 S. Bai, X. Wang, X. Hu, M. Xie, J. Jiang and Y. Xiong, *Chem. Commun.*, 2014, **50**, 6094–6097.
6 C. M. Li, Y. Xu, W. G. Tu, G. Chen and R. Xu, *Green Chem.*, 2017, **19**, 882–899.
7 Z. Tong, D. Yang, Z. Li, Y. Nan, F. Ding and Y. Shen, *ACS Nano*, 2017, **11**, 1103–1112.
8 D. D. Zheng, C. J. Huang and X. C. Wang, *Nanoscale*, 2015, **7**, 465–470.
9 H. N. Che, C. B. Liu, W. Hu, H. Hu, J. Q. Li, J. Y. Dou, W. D. Shi, C. M. Li and H. J. Dong, *Catal. Sci. Technol.*, 2018, **8**, 622–631.
10 Y. Y. Kang, Y. Q. Yang, L. C. Yin, X. D. Kang, L. Z. Wang, G. Liu and H. M. Cheng, *Adv. Mater.*, 2016, **28**, 6471–6477.
11 L. J. Fang, Y. H. Li, P. F. Liu, D. P. Wang, H. D. Zeng, X. L. Wang and H. G. Yang, *ACS Sustainable Chem. Eng.*, 2017, **5**, 2039–2043.
12 Z. C. Sun, M. S. Zhu, M. Fujitsuka, A. J. Wang, C. Shi and T. Majima, *ACS Appl. Mater. Interfaces*, 2017, **9**, 30583–30590.
13 Z. Zhou, Y. Zhang, Y. Shen, S. Liu and Y. Zhang, *Chem. Soc. Rev.*, 2018, **47**, 2298–2321.
14 M. Wang, P. Y. Guo, Y. Zhang, C. M. Lv, T. Y. Chai, Y. H. Xie, Y. Z. Wang and T. Zhu, *J. Hazard. Mater.*, 2018, **349**, 224–233.
15 Z. Xie, Y. Feng, F. Wang, D. Chen, Q. Zhang, Y. Zeng, W. Lv and G. Liu, *Appl. Catal., B*, 2018, **229**, 96–104.
16 Z. Mo, H. Xu, Z. G. Chen, X. J. She, Y. H. Song, J. J. Wu, P. G. Yan, L. Xu, Y. C. Lei, S. Q. Yuan and H. M. Li, *Appl. Catal., B*, 2018, **225**, 154–161.
17 Y. Z. Hong, Y. H. Jiang, C. S. Li, W. Q. Fan, X. Yan, M. Yan and W. D. Shi, *Appl. Catal., B*, 2016, **180**, 663–673.
18 Z. Zhu, Z. Y. Lu, D. D. Wang, X. Tang, Y. S. Yan, W. D. Shi, Y. S. Wang, N. L. Gao, X. Yao and H. J. Dong, *Appl. Catal., B*, 2016, **182**, 115–122.
19 X. J. Bai, S. C. Yan, J. J. Wang, L. Wang, W. J. Jiang, S. L. Wu, C. P. Sun and Y. F. Zhu, *J. Mater. Chem. A*, 2014, **2**, 17521–17529.
20 Y. Wang, J. S. Zhang, X. C. Wang, M. Antonietti and H. R. Li, *Angew. Chem., Int. Ed.*, 2010, **49**, 3356–3359.
21 A. Dailly and E. Poirier, *Energy Environ. Sci.*, 2011, **4**, 3527–3543.
22 F. J. Ma, S. X. Liu, C. Y. Sun, D. D. Liang, G. J. Ren, F. Wei, Y. G. Chen and Z. M. Su, *J. Am. Chem. Soc.*, 2011, **133**, 4178–4181.
23 H. K. Chae, D. Y. Siberio-Perez, J. Kim, Y. Go, M. Eddaoudi, A. J. Matzger, M. O'Keeffe and O. M. Yaghi, *Nature*, 2004, **427**, 523–527.
24 Y. Qiao, Y. F. Ma, W. Jiang, X. Y. Wang, W. S. Guan, G. B. Che, W. K. Li and F. Qin, *CrystEngComm*, 2018, **20**, 7782–7794.
25 J. D. Xiao, Q. C. Shang, Y. J. Xiong, Q. Zhang, Y. Luo and S. H. Yu, *Angew. Chem., Int. Ed.*, 2016, **128**, 9389–9393.
26 W. Xu, Z. X. Si, M. Xie, L. X. Zhou and Y. Q. Zheng, *Cryst. Growth Des.*, 2017, **17**, 2147–2157.
27 P. Li, N. A. Vermeulen, C. D. Malliakas, D. A. G. Gualdrón, A. J. Howarth, B. L. Mehdi, A. Dohnalkova, N. D. Browning, M. O'Keeffe and O. K. Farha, *Science*, 2017, **356**, 624–627.
28 Z. M. Li, Y. Qiao, C. B. Liu, Y. F. Zhou, X. Y. Wang, P. A. Charpentier, G. B. Che, W. Z. Xu, L. H. Liu and E. W. Zhu, *Dalton Trans.*, 2018, **47**, 7761–7775.
29 E. Barea, C. Montoro and J. A. R. Navarro, *Chem. Soc. Rev.*, 2014, **43**, 5419–5430.
30 H. Wang, X. Z. Yuan, Y. Wu, G. M. Zeng, X. H. Chen, L. J. Leng, Z. B. Wu, L. B. Jiang and H. Li, *Appl. Catal., B*, 2015, **174**, 445–454.
31 J. He, Z. Y. Yan, J. Q. Wang, J. Xie, L. Jiang, Y. M. Shi, F. G. Yuan, F. Yu and Y. J. Sun, *Chem. Commun.*, 2013, **49**, 6761–6763.
32 R. Liang, L. J. Shen, F. F. Jing, N. Qin and L. Wu, *ACS Appl. Mater. Interfaces*, 2015, **7**, 9507–9515.
33 S. C. Yan, Z. S. Li and Z. G. Zou, *Langmuir*, 2009, **25**, 10397–10401.
34 H. Wang, X. Z. Yuan, Y. Wu, G. M. Zeng, X. H. Chen, L. J. Leng, Z. B. Wu, L. B. Jiang and H. Li, *J. Hazard. Mater.*, 2015, **286**, 187–194.
35 G. Cheng, M. S. Akhtar, O. B. Yang and F. J. Stadler, *ACS Appl. Mater. Interfaces*, 2013, **5**, 6635–6642.
36 Q. J. Xiang, J. G. Yu and M. Jaroniec, *J. Phys. Chem. C*, 2011, **115**, 7355–7363.
37 J. H. Liu, T. K. Zhang, Z. C. Wang, G. Dawson and W. Chen, *J. Mater. Chem.*, 2011, **21**, 14398–14401.
38 J. X. Sun, Y. P. Yuan, L. G. Qiu, X. Jiang, A. J. Xie, Y. H. Shen and J. F. Zhu, *Dalton Trans.*, 2012, **41**, 6756–6763.
39 X. P. Sun, S. J. Dong and E. Wang, *Angew. Chem., Int. Ed.*, 2004, **43**, 6360–6363.
40 S. W. Zhang, J. X. Li, X. K. Wang, Y. S. Huang, M. Y. Zeng and J. Z. Xu, *ACS Appl. Mater. Interfaces*, 2014, **6**, 22116–22125.
41 Q. X. Luo, B. W. An, M. Ji, S. E. Park, C. Hao and Y. Q. Li, *J. Porous Mater.*, 2015, **22**, 247–259.

42 J. H. Liu, T. K. Zhang, Z. C. Wang, G. Dawson and W. Chen, *J. Mater. Chem.*, 2011, **21**, 14398–14401.
43 F. Dong, L. W. Wu, Y. J. Sun, M. Fu, Z. B. Wu and S. C. Lee, *J. Mater. Chem.*, 2011, **221**, 15171–15174.
44 J. H. Liu, Y. W. Zhang, L. H. Lu, G. Wu and W. Chen, *Chem. Commun.*, 2012, **48**, 8826–8828.
45 Y. J. Wang, X. J. Bai, C. S. Pan, J. He and Y. F. Zhu, *J. Mater. Chem.*, 2012, **22**, 11568–11573.
46 H. H. Yin, K. Yu, C. Q. Song, R. Huang and Z. Q. Zhu, *ACS Appl. Mater. Interfaces*, 2014, **6**, 14851–14860.
47 Z. W. Tong, D. Yang, T. X. Xiao, Y. Tian and Z. Y. Jiang, *Chem. Eng. J.*, 2015, **260**, 117–125.
48 D. Li, Z. D. Wu, C. S. Xing, D. L. Jiang, M. Chen, W. D. Shi and S. Q. Yuan, *J. Mol. Catal. A: Chem.*, 2014, **395**, 261–268.
49 Y. J. Lin, S. Zhou, X. H. Liu, S. Sheehan and D. W. Wang, *J. Am. Chem. Soc.*, 2009, **131**, 2772–2773.
50 W. D. Zhang, L. C. Jiang and J. S. Ye, *J. Phys. Chem. C*, 2009, **113**, 16247–16253.
51 W. R. Zhao, Y. Wang, Y. Yang, J. Tang and Y. Yang, *Appl. Catal., B*, 2012, **115**, 90–99.
52 J. Di, J. X. Xia, S. Yin, H. Xu, L. Xu, Y. G. Xu, M. Q. He and H. M. Li, *J. Mater. Chem. A*, 2014, **2**, 5340–5351.
53 Z. A. Huang, Q. Sun, K. L. Lv, Z. H. Zhang, M. Li and B. Li, *Appl. Catal., B*, 2015, **164**, 420–427.
54 D. S. Wang, H. T. Sun, Q. Z. Luo, X. L. Yang and R. Yin, *Appl. Catal., B*, 2014, **156**, 323–330.
55 W. J. Li, D. Z. Li, Y. M. Lin, P. X. Wang, W. Chen, X. Z. Fu and Y. Shao, *J. Phys. Chem. C*, 2012, **116**, 3552–3560.
56 H. T. Ren, S. Y. Jia, Y. Wu, S. H. Wu, T. H. Zhang and X. Han, *Ind. Eng. Chem. Res.*, 2014, **53**, 17645–17653.
57 M. Xu, L. Han and S. J. Dong, *ACS Appl. Mater. Interfaces*, 2013, **5**, 12533–12540.